AIRIS WIDE AREA DETECTION SYSTEM

William J. Marinelli, Christopher M. Gittins, and Teoman E. Ustun
Physical Sciences Inc.
20 New England Business Center
Andover, MA 01810

James O. Jensen
U.S. Army SBCCOM
5183 Blackhawk Road
Aberdeen Proving Ground, MD 21010-5424

ABSTRACT

The AIRIS Wide Area Detection System was employed, in both airborne and ground-based configurations, to detect chemical and biological agent stimulant releases during the Technology Readiness Evaluations conducted at Dugway Proving Grounds from 22-26 July 2002. Airborne observations were conducted from a gyro-stabilized pointing system mounted on a UH-1 helicopter and conducted at ranges up to ~ 7 km and altitudes to 1600 ft in conjunction with the Redstone Technical Test Center. Ground-based observations were made at ranges between 1 and 5 km. The sensors comprised 64 x 64 element HgCdTe detector arrays coupled to AIRIS tunable filters resulting in a system with nominal 10 cm^{-1} spectral resolution and a 0.8 milliradian IFOV. The measured NESR for these systems ranged from 2 to 3 $\mu W/(cm^2\ sr\ \mu m)$. Observations were made of the biological simulants BG and erwinia herbicola, the chemical stimulant SF_6, as well as the interferents kaolin clay dust, Dugway road dust, and diesel soot. In this paper we will report on quantitative observations of these releases.

INTRODUCTION

In this paper we describe the results of ground and airborne imaging experiments involving an LWIR imaging Fabry-Perot spectrometer developed by Physical Sciences Inc. (PSI). The instruments are known as Adaptive InfraRed Imaging Spectroradiometers, *AIRIS*™, U.S. Patent 5,461,477. The experiments involved imaging a series controlled chemical vapor and biological aerosol releases at the US Army Dugway Proving Grounds. Airborne measurements were conducted using an AIRIS system contained in a pod, known as "Fat Boy," mounted on a UH-1 helicopter. Observations of releases we made at ranges as great as 5 km on tracks moving both upwind and downwind with respect to the release point. Ground-based measurements were conducted from a fixed location with releases occurring at ranges from 1 to 5 km.

Report Documentation Page

Form Approved
OMB No. 0704-0188

1. REPORT DATE	2. REPORT TYPE	3. DATES COVERED
01 JUL 2003	**N/A**	**-**

4. TITLE AND SUBTITLE	5a. CONTRACT NUMBER
AIRIS Wide Area Detection System	5b. GRANT NUMBER
	5c. PROGRAM ELEMENT NUMBER
6. AUTHOR(S)	5d. PROJECT NUMBER
	5e. TASK NUMBER
	5f. WORK UNIT NUMBER
7. PERFORMING ORGANIZATION NAME(S) AND ADDRESS(ES) **Physical Sciences Inc. 20 New England Business Center Andover, MA 01810**	8. PERFORMING ORGANIZATION REPORT NUMBER
9. SPONSORING/MONITORING AGENCY NAME(S) AND ADDRESS(ES)	10. SPONSOR/MONITOR'S ACRONYM(S)
	11. SPONSOR/MONITOR'S REPORT NUMBER(S)

12. DISTRIBUTION/AVAILABILITY STATEMENT
Approved for public release, distribution unlimited

13. SUPPLEMENTARY NOTES
See also ADM001523.

14. ABSTRACT

15. SUBJECT TERMS

16. SECURITY CLASSIFICATION OF:			17. LIMITATION OF ABSTRACT	18. NUMBER OF PAGES	19a. NAME OF RESPONSIBLE PERSON
a. REPORT	b. ABSTRACT	c. THIS PAGE			
unclassified	**unclassified**	**unclassified**	**UU**	**8**	

EQUIPMENT AND METHODS

Passive sensing of CB stimulant releases requires exploitation of both the spectral signatures of the target species as well as the radiance contrast between the release plume and the background scene. The imaging spectrometers employed in these measurements are comprised of an LWIR focal plane array-based camera which views the far field through a low-order, tunable Fabry-Perot etalon. The tunable etalon provides the spectral resolution necessary to resolve structured absorption and emission from molecular vapors and aerosols. The focal plane array (FPA) enables radiance measurements of sufficient accuracy that chemical vapors and aerosols may be selectively detected with only several degrees effective temperature difference between the vapor and the background.

We analyze the multispectral imaging data using algorithms developed at PSI. Previously, we have shown two key sensor capabilities:

- Selective detection of one and two chemical species in plumes containing multiple species
- Detection of a single species with low false alarm rate using a limited number of detection bands.

This paper highlights our observations of bacillus subtilis aerosols and SF_6 chemical plumes against a terrestrial backgrounds.

A schematic illustration of the complete AIRIS optical train is depicted in Figure 1. The sensor design was developed by PSI and is described in prior publications.[1,2]

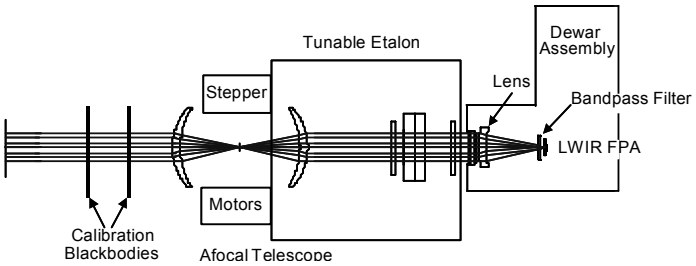

Figure 1. Schematic illustration of AIRIS optical train.

The Fabry-Perot interferometer (etalon) enables the sensors' hyperspectral capabilities. It operates as a tunable interference filter which selects the wavelength that illuminates the FPA. This configuration affords both wide field-of-view and broad spectral coverage. A bandpass filter is placed in front of the FPA to limit its response to a single etalon transmission order. There are ~40 spectral resolution elements over the interferometer's operating range. The spacing and alignment of the etalon mirrors are controlled via a closed-loop control system. The etalon can be tuned between resolution elements in 20 to 30 ms while maintaining wavelength positioning accuracy of ~1 cm^{-1}. The AIRIS system control program is derived from the software used to control the instrument's LWIR camera. Etalon control is accomplished within the system control program. Each AIRIS system computer is an Intel Pentium-based PC with Windows NT 4.0 as the operating system.

The airborne experiments were scheduled to use a 256 x 256 pixel format HgCdTe array in the AIRIS system. The sensor employing this array was extensively tested in pre-TRE flight testing at the Redstone Technical Test Center in Huntsville, AL. However, a failure of that array after initial flight testing led to the substitution of a similar array with only a 64 x 64 pixel format. Table 1 lists the salient characteristics of each instrument's camera and optical train.

The 50 mm Ge lens located in front of the FPA results in an f/2.4 optical train. The lens provides diffraction limited focal spot size (~1 pixel) on-axis and ~2 pixels blurring (astigmatism) at the corners of the 64 x 64 pixel FPA. The 3:2 afocal telescope located beyond the tunable etalon module provides a fine adjustment of the system focus. Two calibration blackbodies are mounted on a rotation stage and enable collection of radiometric calibration data. The high temperature blackbody is normally operated 10 to 15 K above ambient temperature and the low temperature blackbody operated ~5 K below ambient. The blackbodies are used to generate two point radiometric calibrations (gain and offset) for each pixel at each wavelength viewed. The calibration blackbodies are rotated clear of the system field-of-view during normal operation.

Table 1. AIRIS-CW Characteristics

Property \ Instrument	64 x 64 FPA-Based	256 x 256 FPA-Based
Pixel pitch [μm]	61	40
Afocal telescope magnification	3:2	3:2
IFOV [mrad]	0.80	0.53
Field-of-regard [deg x deg]	3.0 x 3.0	7.8 x 7.8
FPA readout	rolling	snapshot
Camera frame rate [Hz]	21.3	114.9
FPA integration time [ms (typ.)]	1.44	0.56
A/D dynamic range [bits]	14	14

In airborne operations the entire optical train is mounted on a servo-controlled optical bench slaved to a pointing and tracking system that allows the operator to lock on to a specific point on the ground and obtain multispectral data over the system field of view. Figure 2 shows a detailed view of the sensor in the Fat Boy. Electronics to operate the system were mounted in a rack system located in the passenger/cargo compartment of the UH-1 with cables running through the rack to the ball through a bundle strapped to the aircraft exterior.

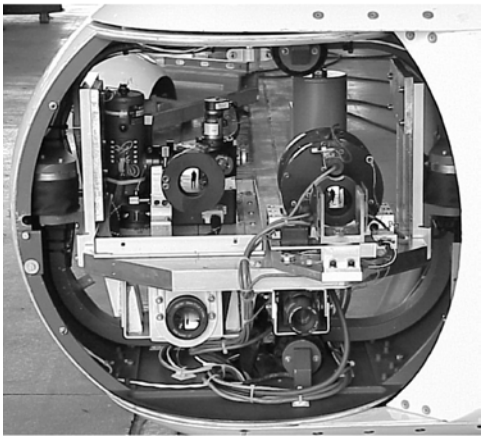

Figure 2. Photograph of Fat Boy with aerodynamic skins off showing AIRIS-LW (upper right, Turbo-FT (upper left), IR camera for tracking (lower left) and intensified visible camera for tracking (lower right).

SYSTEM OPERATION

Data acquisition during the Airborne TRE experiments was accomplished, for the most part, by locking the Fat Boy tracking system on to a fixed location on the ground at or downwind of the test site and then acquiring spectral data cubes during the releases as the UH-1 slowly (typically 10 to 20 kt) traversed either upwind or downwind with respect to the release point.

The FAT Boy was limited to look down angles of 22.5 degrees from horizontal. The typical flight altitude was 300 meters, resulting in a minimum standoff distance of approximately 750 meters. The terrain at the site is one of desert floor, sparsely covered by scrub brush with a height of approximately 2 ft.

Releases occurred over periods as long as 5 minutes. Prior to each release the system was calibrated radiometrically using the two on-board blackbody calibrators. As many as 8 data cubes were acquired during a typical data collection pass. However, on several of the data cubes the tracking system would jitter and loose lock during acquisition events due to the low contrast in the scene, leading to a shift in the location of the target in the image with each wavelength image in the data cube. This paper focuses on the analysis of those data cubes where the shift in the imagery was negligible, i.e., there was no apparent shift in the spatial location of the blackbody emission from the release vehicle throughout the data cube. The goals of the airborne measurements were to:

1. Demonstrate airborne operation of the AIRIS sensor and
2. Demonstrate the ability to detect chemical and biological agent stimulant releases from airborne and ground platforms.

Due to problems with the 256 x 256 FPA no airborne data was acquired on BW stimulant releases. Operation of the system with the 64 x 64 element FPA was successful in all respects. This array was slower framing than the 256 x 256 system (11 seconds vs 1 second to collect a data cube), making the data more susceptible to tracking jitter in the Fat Boy. However, the 64 x 64 element array has response that extends to 11 μm whereas the 256 x 256 element system's response cuts off at about 10.2 μm.

AIRBORNE MEASUREMENT DATA ANALYSIS

The hyperspectral data cubes generated using AIRIS consisted of 36 narrowband images: 1260 cm^{-1} (7.94 μm) to 910 cm^{-1} (10.99 μm) in 10 cm^{-1} increments with the 64 x 64 system. Analysis was conducted by applying the absolute radiometric calibration to the data and then analyzing regions of interest for spectral content. A simple algorithm allowed the user to define a region of the scene representative of the local background and then subtract the background spectrum from each pixel in the data cube to obtain a net change in radiance from the background. This differential radiance data cube was then analyzed for spectral content by looking for matches with the SF_6 spectrum. Subsequently, a spectrally matched filter approach was used to search data cubes for the presence of SF_6 without a priori knowledge of its location in the field of view. Sample data from the data cube 20726c8 is used to illustrate the both approaches. This data cube was acquired during a release of SF_6 that occurred continuously for 5 minutes with a total release of 38 kg or a release rate of 127 grams/second. Wind speed during the release was 1.4 meters/second and turbulence was low.

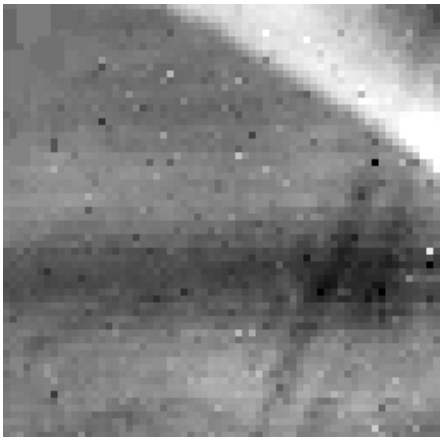

Figure 3. IR image at 10.6 μm showing SF_6 plume crossing top right region of field.

An image of the scene recorded at 10.6 um, at the peak of the SF_6 absorption band, is shown in Figure 3. The data shows a rather monotonic background interrupted by roads seen moving through the scene from bottom center to top right. Note that the roads are darker, and hence apparently cooler that the rest of the scene, which is dominated by the vegetation. While some of this apparent temperature differential may be due to emissivity differences between the two surfaces, it is also true that vegetation more closely reaches the air temperature due to the motion of the wind through the leaves. The upper right corner of the image shows a white streak moving through the scene which can be identified as the plume from the SF_6 release. The region in the top left of the image, outside of the plume area, was used to obtain the background. The spectral data from that region was fit to the Planck blackbody function, assuming unit emissivity, and found to have a radiance temperature of approximately 285 K (11.8°C). Air temperature that evening was measured to be 25°C; hence an apparent ΔT of approximately 13 degrees existed between the background and the air.

The subtraction of the background radiance from the entire data cube results in the cancellation of much of the background radiance but not the differential signal from the road underlying the SF_6 release plume.

The net spectrum of the upper region of the scene is shown in Figure 4. The spectrum shows net intensity in the region of 8.0 to 8.5 μm and again from 10 to 11 μm. The intensity at shorter wavelengths is likely due to imprecision in the subtraction of atmospheric absorption, which may be variable, while the intensity at longer wavelengths can be ascribed to SF_6. For illustration purposes a spectrum of SF_6, convolved with the resolution function of the system, has been superimposed on the data in Figure 4. While the fit is far from exact, the data clearly indicates the presence of SF_6 in that region. The spectral feature in the data is somewhat broader than the simulation spectrum. However, it is well known that SF_6

becomes optically thick on its Q-branch feature, which carries most of the absorption band strength, at column densities greater than about 100 ppmv-m. This effect leads to a broadening of the feature and non-Beer's Law behavior at higher column densities for spectral resolutions that cannot resolve the Q-branch, which is the case with the AIRIS system.

For the case of a single chemical species in an optically thin plume, the differential radiance at the sensor with and without the plume present is:

$$\Delta N(\lambda)_{sens} = N_{plume}(\lambda) - N_{bkgd}(\lambda) \approx \sigma(\lambda) \cdot \rho L \cdot \left[\frac{dN}{dT}\right]_{T_{bkgd}} \cdot \Delta T \qquad (1)$$

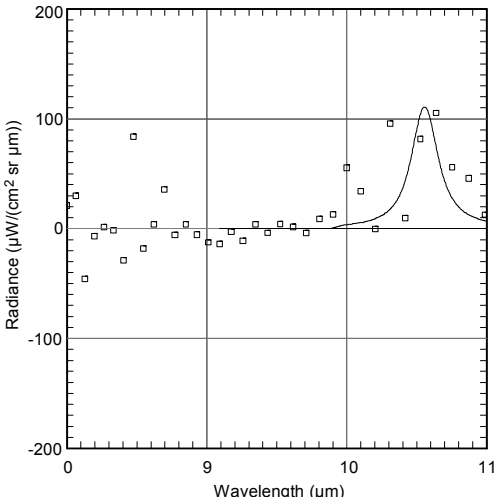

Figure 4. Net radiance spectrum of region containing SF_6 with spectrum of SF_6 superimposed on the data for comparison.

where σ is the chemical's absorption coefficient, ρL is its column density, the quantity in brackets is the derivative of the Planck function with respect to temperature (~16 μW/(cm^2 sr μm K) at 10 μm and 300 K), and ΔT is the effective temperature differential between the plume and the background. The data in Figure 4 shows a differential radiance of about 100 μW/(cm^2 sr^{-1} μm^{-1}) while the SF_6, absorption coefficient, derived from a resolution degraded HITRAN spectrum of SF_6 is 2.5 x 10^{-3} ppmv^{-1} m^{-1}. Inversion of Equation 1 to obtain an apparent SF_6 column density was done assuming a 13K radiance temperature differential, i.e., it was assumed that the SF_6 was equilibrated with the air temperature. This analysis resulted in an assignment of the SF_6 column density of approximately 200 ppmv-m. In future work we hope to correlate this measurement with a Gaussian plume dispersion model of the SF_6 release.

GROUND-BASED BIOLOGICAL SIMULANT RELEASES

In our data analysis we have concentrated on the BG puff release observed from a range of 3 km on the night of July 22/23 (dissemination initiated at ~0203 hours on July 23). We chose to concentrate on that dissemination because the BG puff was visible in the narrowband imagery displayed on the sensor's real-time video monitor. Because the video imagery was observed only at fixed wavelengths before and after data cubes were acquired, it was not apparent whether the signature was a purely thermal effect (BG cloud colder than the background) or whether the cloud exhibited a distinct spectrum. After conducting our preliminary analysis, we conclude that the BG cloud exhibited a distinct signature; however the signature cannot be explained in terms of simple attenuation of background radiation or emission from BG particles.

Figure 5 depicts a narrowband IR image of the puff release area approximately 30 seconds after the dissemination. The apparent location of the BG cloud is encircled by the ellipse. A radio tower several km behind the puff release area can be seen slightly to the left of the center of the image. The horizon line is apparent approximately halfway up the image.

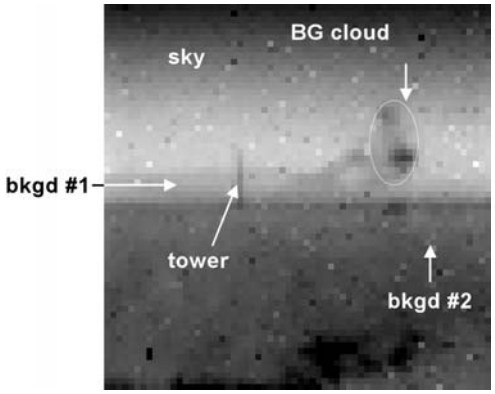

Figure 5. Narrowband image of BG puff release at 10.1 μm. The apparent location of the BG cloud is encircled by the elipse.

Mountains >10 km beyond the radio tower are barely visible above the horizon. The overall scene exhibits only several degrees apparent thermal contrast.

The XM94 referee lidar determined the aerosol concentration to be ~$4 \cdot 10^6$ particles/liter and the cloud height to 25 to 30 meters approximately two minutes after acquisition of the first data cube. The reported cloud height is consistent with the imagery shown in Figure 5. Qualitative analysis of Figure 5 suggests a cloud height of ~14 pixels*0.80 milliradians/pixel*3 km = 34 m. The BG cloud was observed to drift from the center to the far right of the sensor's field-of-view during the acquisition of the data cube. In order to extract the spectrum of the cloud, it was necessary to manually define the cloud location in each narrowband image. (Note: The data cube acquisition rate could be increased by approximately one order of magnitude, and the target motion issue eliminated, by replacing the low cost, rolling readout FPA used in this AIRIS with a snapshot-capable FPA.) We selected a 3 x 3 pixel block in each image for determination of the cloud spectrum. At the wavelengths where the cloud was visible in the narrowband imagery, its spatial extent was greater than 3 x 3 pixels.

The algorithm used to analyze the imaging performs a statistical analysis the full hyperspectral data cube to infer the "background" spectrum at each pixel. The statistically inferred background is then subtracted from the data to generate a differential radiance spectrum. Automated target detection is accomplished by comparing the differential radiance spectrum with a reference spectrum of the target. (This analysis approach is extremely effective when the target occupies a small fraction of the image, as was the case during the TRE02 disseminations.) In our preliminary analysis, we have examined differential radiance spectra of the BG cloud as well as pure background areas in the scene. Figure 6 depicts differential radiance spectra of the BG cloud and the areas labeled "bkgd #1" and "bkgd #2" in Figure 5. The BG cloud exhibits a broad feature which peaks at ~10.3 μm. The observed differential radiance at 10.3 μm is equivalent to a -0.8 K temperature change from a blackbody with $\varepsilon = 1$.

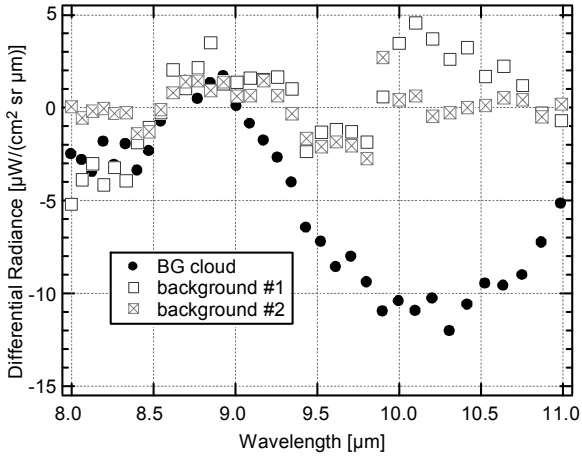

Figure 6. Differential radiance spectra of BG cloud and two areas identified as background in Figure 5.

The origin of the signature observed from the BG cloud can be understood by considering the scattering as well as the absorption properties of these particles. The relevant processes are illustrated in Figure 7, where the upper section (Mechanism 1) illustrates that the extinction (or attenuation) of radiation incident on the cloud from the background includes both direct absorption as well as scattering to the surroundings. The center section of Figure 7 (Mechanism 2) shows conventional direct emission of radiation from the cloud to the sensor. The lower panel of the figure illustrates the scattering of radiation from the earth and sky environment in which the cloud is located, with some component of that radiation reaching the sensor (Mechanism 3). In an isotropic and isothermal environment the scattering processes defined by Mechanism 1 would be exactly balanced by the processes in Mechanism 3 and the thermal signature of the cloud would be determined by the traditional mechanisms embodied in chemical detection problems. However, only 20 to 40% of the total extinction in the thermal IR region by BG particles is due to absorption. Furthermore, in the field on a clear night, a significant fraction of the solid angle subtended by the cloud is cold sky. Therefore, at wavelengths where scattering is significant, near ambient temperature radiation from the background scattered to the cold sky is replaced by a lesser amount of radiation originating from that source. This process leads to a reduction in the apparent thermal emission of the particles at those wavelengths.

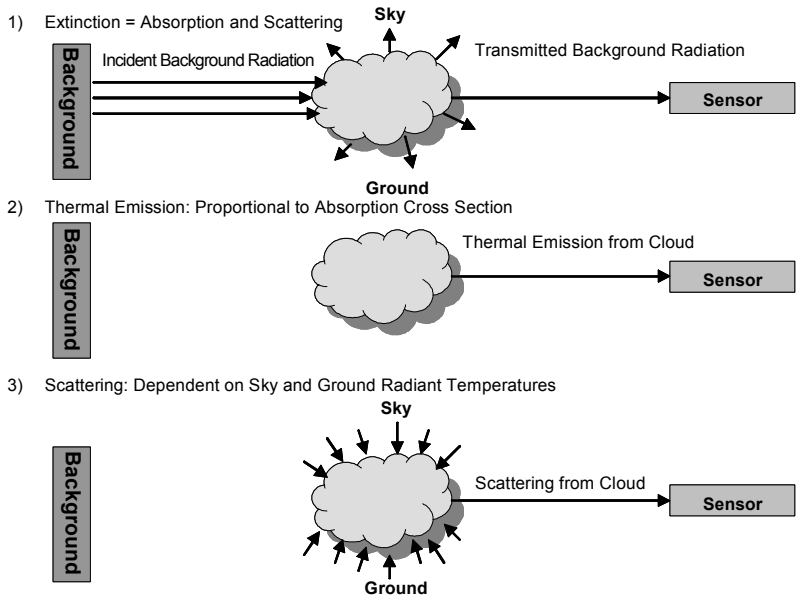

Figure 7. Schematic diagram of the mechanisms responsible for the generation of the thermal infrared signature of the BG cloud. See the test for an explanation of the mechanisms.

This concept was placed on a quantitative basis by using the known real and imaginary refractive indexes of BG as a function of wavelength[3,4] to calculate the extinction, scattering, and absorption cross sections of BG particles using Mie scattering calculations. The calculations assume the particles are spore agglomerates that assume a spherical form. The ratio of extinction to absorption cross sections as a function of wavelength for a log-normal BG particle distribution with a mean diameter of 3 μm and a width of 3 μm is shown in Figure 8. This function is of the same form as the wavelength dependence of the differential radiance signal seen from the BG cloud in Figure 6.

These cross sections were then used in an expanded three-layer model of radiative transfer through the cloud that incorporates scattering of radiation originating from two horizontal layers (sky and ground) subtending 4 and 8.5 steradians respectively. For simplicity, the radiance of these sources as function of wavelength was defined to be Planck functions with unit emissivity and characteristic temperatures of 294 K and 250 K respectively. These temperatures were derived from measurements conducted with a thermal infrared optical thermometer pointed at the ground and sky. The radiative transfer model ignores any angular dependence of the scattering cross sections, making the assumption that these effects are averaged over the large solid angles subtended by the radiation sources. The predicted signature for the cloud at a range of 3 km is shown in Figure 9 for an air temperature of 298 K and a particle density of 150 cm^{-3}. The calculation is in good agreement with the data in both magnitude and variation as a

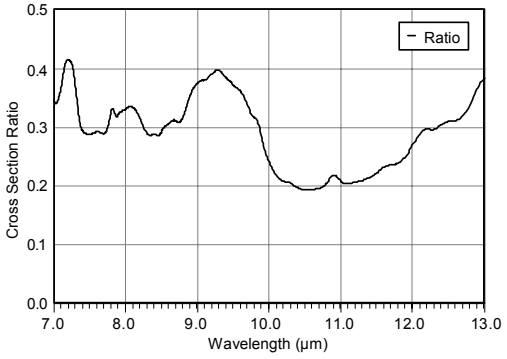

Figure 8. Wavelength dependence of the ratio of absorption to extinction cross sections for BG particles with a 3 μm mean diameter and 3 μm mean log-normal distribution width.

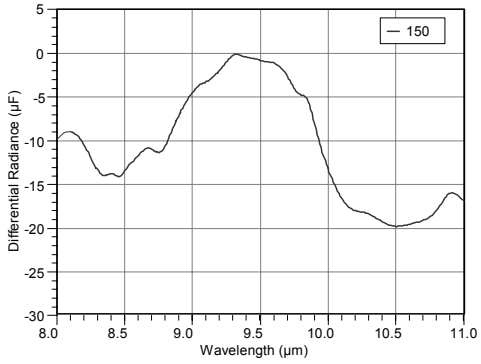

Figure 9. Calculated differential radiance signal as a function of wavelength using the extended radiative transfer model incorporating scattering and the parameters of the measurement shown in Figure 6.

function of wavelength, indicating a high probability that this mechanism is the primary source of the cloud thermal signature. Additional Mie scattering calculations demonstrate that the wavelength dependence of the signature should be a very weak function of the mean particle diameter as well as the width of the log-normal distribution. However, the absolute magnitude of the cross sections scale roughly linearly with particle diameter. Thus, on a mass-normalized basis the signature should be much more sensitive to smaller diameter particles (finely divided spore particles) and less sensitive to large particles, such as pollens.

CONCLUSIONS

Our review of the results of the AIRIS sensor testing conducted during the Technology Readiness Evaluations in July of 2002 showed that the system functioned well in a high vibration environment over a wide range of operational temperatures. From our analysis of the data we conclude the following:

- The system definitively detected SF_6 releases with column densities at the 200 ppmv-m level from an airborne platform in many data sets. The plumes were detected using both manual analysis as well as using an automated spectrally matched filter approach.

- A signal was observed in the infrared imagery during the puff releases of BG at a range of 3 km. This signal has been analyzed and can be understood in both form and magnitude by considering both absorption and scattering by the BG aerosol cloud. This signal could be used to discriminate BG from other non-biological aerosols during releases using existing passive infrared systems.

The data supports the continued development of passive multispectral imaging technologies to address wide area standoff chemical and biological agent detection needs.

REFERENCES

1. C.M.Gittins, W.J.Marinelli, and J.O.Jensen, "Remote Characterization of Chemical Vapor Plumes by LWIR Imaging Fabry-Perot Spectrometry," in *Proc. of the Int. Symp. on Spectral Sensing Research*, Quebec City, 11-15 June 2001, p.294-302.
2. C.M.Gittins, W.J.Marinelli, and J.O.Jensen, "Remote Sensing and Selective Detection of Chemical Vapor Plumes by LWIR Imaging Fabry-Perot Spectrometry," *Proc. SPIE* **4574**, p.63-73 (2002).
3. Querry, M.R., private communication of data from Merrill Milham (1999).
4. Tuminello, P.S., Arakawa, E.T., Khare, B.N., Wrobel, J.M., Querry, M.R., and Milham, M.E., "Optical Properties of Bacillus Subtilis Spores from 0.2 to 2.5 μm," *Applied Optics*, *36*, 13 (1997).